Appendix A

Quantum models

Quantum models based on specific structures and established distances are implemented for deterministic models from the perspective of quantum physics [1, 2]. Presently, models based on characteristics of quantum physical chemistry provide viable non-deterministic predictive alternatives, but models are complex and combine more than two theories. In this case, the model theory of quantum fields is presented, through the Lorentz model, applied in a chitosan molecule with ramifications and its interaction with Ag_2ONPs.

Lorentz model

The Lorentz model is implemented to observe the deformation of the electromagnetic field in the studied molecules, this can be compared with quantum models [3]. From the Lorentz field equation (Eq. 1):

$$\boldsymbol{F} = q(\boldsymbol{E} + \mathbf{v} \times \boldsymbol{B}) \qquad (1)$$

F denotes the strength of the electromagnetic field, E and B are vectors of both fields and v is the velocity of the particle. For a continuous field, Eq. 1 is modified, obtaining Eq. 2:

$$d\boldsymbol{F} = dq(\boldsymbol{E} + \mathbf{v} \times \boldsymbol{B}) \qquad (2)$$

Where the electromagnetic field is adjusted as a function of the current density

$$J = \varphi v \qquad (3)$$

For a volume change in an electromagnetic field, F can be denoted as Eq. (4):

$$F = \iiint (\varphi E + J \times B) dV \qquad (4)$$

Instead, from the Maxwell-Faraday relationship for the charge induction in an electromagnetic field, we have Eqs. 5 and 6:

$$\nabla \times E = -\frac{\partial B}{\partial t} \qquad (5)$$

$$F = qE(r,t) + qv \times B(r,t) \qquad (6)$$

Furthermore, Equation 7 is obtained from the dispersion of the induced field in a control volume.

$$\oint_{\partial\Sigma(t)} d\ell \cdot \frac{F}{q(r,t)} = \oint_{\partial\Sigma(t)} d\ell \cdot E(r,t) + \oint_{\partial\Sigma(t)} v \cdot B(r,t) d\ell \qquad (7)$$

For the electron scattering within the electromagnetic field of the molecular structure, it is employed Eq. 8:

$$F = q\left[-\nabla_x(\phi - \dot{x}\cdot A) + \frac{d}{dt}\nabla_{\dot{x}}(\phi - \dot{x}\cdot A)\right] \quad (8)$$

According to quantum mechanics, the Schrödinger equation is required for modeling the surface of a structurally balanced molecule; therefore, the model of the functional theory of density is proposed in Eq. 9.

$$\frac{\hbar^2}{2m}\frac{\partial^2\Psi(x,t)}{\partial x^2} + U(x,t)\Psi(x,t) = i\hbar\frac{\partial\Psi(x,t)}{\partial t} \quad (9)$$

Where the potential energy can be replaced by the electromagnetic field equation (Eq. 8) and the distribution of the induced field which corresponds to Eq. 10.

$$U(x,t) = qE(r,t) + qv\times B(r,t) + q\left[-\nabla_x(\phi - \dot{x}\cdot A) + \frac{d}{dt}\nabla_{\dot{x}}(\phi - \dot{x}\cdot A)\right] \quad (10)$$

Substituting Eq. 10 into the Schrödinger equation (Eq. 9), we get the following equation (11):

$$\frac{\hbar^2}{2m}\frac{\partial^2\Psi(x,t)}{\partial x^2} + qE(r,t) + qv\times B(r,t) + q\left[-\nabla_x(\phi - \dot{x}\cdot A) + \frac{d}{dt}\nabla_{\dot{x}}(\phi - \dot{x}\cdot A)\right]\Psi(x,t) = i\hbar\frac{\partial\Psi(x,t)}{\partial t} \quad (11)$$

The nonrelativistic time-independent Schrödinger equation (Eq. 9) establishes the basic expression for any further theoretical consideration, depicted in Eq. 12.

$$\hat{H}\Psi = E\Psi \quad (12)$$

Where the general notation for the Schrödinger equation consists of the Hamiltonian $\hat{H}$, the energy E and the wave function Ψ, which is an eigenfunction of the Hamiltonian [4]. Hence, the Schrödinger equation represents an eigenvalue problem, which is illustrated in Eq. 13.

$$\hat{H}\Psi = qE(r,t) + qv\times B(r,t) + q\left[-\nabla_x(\phi - \dot{x}\cdot A) + \frac{d}{dt}\nabla_{\dot{x}}(\phi - \dot{x}\cdot A)\right]\Psi \quad (13)$$

On the other hand, the main idea of the Born-Oppenheimer approximation derives from the great difference between electrons and nuclei concerning their mass. Compared to an electron, the mass of a nucleus is much higher, and hence the motion of nuclei is significantly slower. In concordance with the first approximation, the motion of the nuclei occurs in the effective potential V_{eff} of the electrons eq. 14.

$$V_{eff} = \left[\frac{\hbar}{2m}\sum_{i=1}^{N}\nabla_i^2 + \sum_{i=1}^{N}\vec{V}(\vec{r_i}) + \sum_{i=1}^{N}\sum_{j<i}^{N}U(\vec{r_i},\vec{r_j})\,\Psi\right] \quad (14)$$

Where the first term corresponds to the kinetics energy of each electron, the second term corresponds to the energy of interaction of the electron with the group of nuclei and the third term to the energy of interaction between the different electrons.

For this reason, the wave function for such system can be divided into two parts, which are the electronic Ψ^{elec} (r) and the nuclear wave function Ψ^{nucl} (R), as shown in eq. 15. The position of the nuclei and the electrons is thereby given by the vectors **R** and **r**.

$$\Psi = \Psi^{elec}(\mathbf{r},\mathbf{R}) \cdot \Psi^{nucl}(\mathbf{R}) \qquad (15)$$

The electronic wave function describes the electron motion depending on the electron coordinates **r** for a given set of nuclei coordinates **R**. Thus, the electronic wave function Ψ^{elec} (**r**,**R**) parametrically depends on the arrangement of the nuclei. Consequently, the electronic Hamiltonian in eq. 16 and the electronic Schrödinger (eq. 17) within the Born-Oppenheimer approximation can be observed.

$$\widehat{H}^{elec} = -\sum_{i=1}^{N} \frac{1}{2}\nabla_i^2 - \sum_{i=1}^{N}\sum_{A=1}^{M} \frac{Z_A}{r_{iA}} + \sum_{i=1}^{N}\sum_{j>i}^{N} \frac{1}{r_{ij}} \qquad (16)$$

$$\widehat{H}^{elec}\Psi^{elec}(r,R) = E^{elec}(R)\Psi^{elec}(r,R) \qquad (17)$$

The DMol^3 module allows to model the electronic structure and energetics of organic and inorganic materials as the chitosan and metallic nanoparticles. The "total energy" of a molecule or crystal refers to the energy of a specific arrangement of atoms as calculated using eq. 18.

$$E_t[\rho] = \sum_i \left\langle \phi_i \left| -\frac{\nabla^2}{2} \right| \phi_i \right\rangle + \langle \rho(r_1) \left[\mu_{xc}[\rho(r_1)] + \frac{V_e(r_1)}{2} + V_N \right] \rangle + E_{NN} \qquad (18)$$

To determine the actual energy variations in E_t, it must be optimized with respect to variations in ρ, subject to the orthonormality constraints in eq. 19.

$$E_t[\rho] = T[\rho] + U[\rho] + E_{xc}[\rho] \qquad (19)$$

Where:

T[ρ] is the kinetics energy of a system of non-interacting particles of density ρ.

U[ρ] is the classical electrostatic energy due to Coulombic interactions.

E_{xc}[ρ] includes all many-body contributions to the total energy, in particular, the exchange and correlation energies.

The charge density is constructed from a wave function Ψ. As in other molecular orbital methods [5], the wave function is taken to be an anti-symmetrized product of one-particle functions, in this case molecular orbitals (MOs) represented in eq. 20.

$$\Psi = \frac{1}{\sqrt{n!}}(n)|\phi_1(1)\phi_1(2) \dots \phi_n(n)| \qquad (20)$$

The obtained density from this expression is also known as the charge density. The MOs may be occupied by two different types of electrons: the ones that are spin-up (alpha) or the seconds that are spin-down (beta). The same ϕ_i for both alpha and beta electrons is known as a spin-restricted calculation; using different ϕ_i for alpha and beta electrons results in a spin-unrestricted or spin-polarized calculation. In the unrestricted case, it is possible to form two different charge densities: one for the alpha MOs and the other for the beta MOs. Their sum gives the total charge density, and their difference gives the spin density, *i.e.*, the amount of excess of the alpha spin over the beta spin. This is analogous to the restricted and unrestricted Hartree-Fock theory [6]. The total energy is obtained from eq. 18. To determine the actual energy, variations in E_t must be optimized with respect to variations in ρ, subject to the orthonormality constraints in eq. 21.

$$\rho(\vec{r}) = N \int d^3r_2 \int d^3r_3 \cdots \int d^3r_N \Psi^*(\vec{r}, \vec{r}_2, \cdots \vec{r}_N) \qquad (21)$$

The atomic orbitals χ_μ are called the atomic basis functions and the $C_{i\mu}$ are the ϕ expansion coefficients. Several choices are possible for the basic set, including Gaussian functions [7], Slater functions [8] plane waves [9] and numerical orbitals. Unlike the MOs, the AOs are not necessarily orthonormal [10]. This leads to a reformulation of eq. 17 in the form of eq. 22.

$$HC = \epsilon SC \qquad (22)$$

Where

$$H_{\mu\nu} = \left\langle \mathcal{X}_\mu(r_1) \middle| -\frac{\nabla^2}{2} + V_N + V_e + \mu_{xc}[\rho(r_1)] \middle| \mathcal{X}_\nu(r_1) \right\rangle \qquad (23)$$

And

$$S_{\mu\nu} = \left\langle \mathcal{X}_\mu(r_1) \middle| \mathcal{X}_\nu(r_1) \right\rangle \qquad (24)$$

Approximations of the Density Functional Theory (DFT) described above have proved to be very successful for most compounds [11, 12]. Nevertheless, they leave a class of so called "strongly correlated" systems beyond their consideration [13]. These systems are usually

described by the simplified body Hamiltonians, which are valid under different circumstances, but cannot efficiently be constructed *ab initio* [14].

The power of these approximations is very attractive and can be refined by considering a one-particle density matrix: n(s,r,s',r') as a basic variable instead of spin density n(s,r). However, such a generalization faces a certain challenge: there are no exactly solvable problems which can be used to parameterize the generalized exchange-correlation energy. Therefore, some models must be used.

Computer calculations

To visualize these models as two-dimensional images and to observe their structure as it would be projected in a transmission electron microscope (TEM), the software SimulaTEM® [9] was employed and its fundamental theory is described below.

To evaluate the integrals, it must be accomplished by a numerical integration procedure, due to the representation of the exchange correlation potential; so, the matrix elements need to be approximated by the finite sums shown in eq. 25.

$$H_\mu \cong \sum_i \mathcal{X}_\mu(r_i) H_{eff}(r_i)\, \mathcal{X}_\upsilon(r_i)\omega(r_i) \qquad (25)$$

The type of systems that can be studied with DFT*, i.e.,* molecules, clusters, or periodic solids are specifically applied to infinite periodic systems [15]. Thus, it is assumed that the system is periodic in three dimensions.

Consider a crystal with lattice vectors a_i, i = 1, 2, 3. For example, in a simple cubic cell, the vectors could be a_1 = (1, 0, 0); a_2 = (0, 1, 0); and a_3 = (0, 0, 1). The basic functions must have the translational symmetry of the crystal, as depicted in eq. 26.

$$\mathcal{X}_\mu(r) = \mathcal{X}_\mu(r + R) \qquad (26)$$

To meet this requirement, a set of plane waves with the periodicity of the lattice is generally introduced and the periodic basis is taken as in eq. 27.

$$\psi(k, r) = e^{ikr}\mathcal{X}(r) \qquad (27)$$

There are, in principle, an infinite number of vectors *k* and *R* needed to describe the exact space. In practice, the number of wave-planes is determined by the cutoff kinetics energy which is chosen to represent physically relevant spatial harmonics of wave functions. The vectors *k* is called *k*-points and are needed to correctly describe the band structure. In practice, only a few *k*-points (in the order of 1-100) are needed. The ability to evaluate the derivative

of the total energy with respect to geometric changes is critical for the study of chemical systems [15-17]. Without the first derivatives, a laborious point-by-point procedure is required, which is taxing to both computer and human resources.

The generalized gradient functional depend on the local density and on the gradients themselves, and its calculation with DMol^3 can handle functional that depend on the kinetics energy density, shown in eq. 28.

$$\tau_i(r) = \sum_i^{ocup} \frac{1}{2} |\nabla \psi_i(r)|^2 \qquad (28)$$

For first-row atoms, functions from +2 ions provide a reasonable double basis set. A hydrogenic 3D orbital obtained for a nucleus of Z = 5 provides a good polarization function for each of these atoms. A hydrogenic 2p function for Z = 1.3 is used for hydrogen. The use of various nuclear charges to generate polarization functions is analogous to the variation of zeta in Gaussian basis sets. For metals, 4p polarization functions are generated by solving the atomic equations for a 4s → 4p excited state. Basis set quality has been analyzed in detail by Delley [18].

The triple numerical set (TNP) has been recently generated and validated by Delley [18]. The evaluation of the integrals in eqs. 23 and 24 must be accomplished by a numerical integration procedure, due to the nature of the basic functions. The matrix elements need to be approximated by the finite sums in eqs. 29, and 30.

$$H_{\mu\nu} \cong \sum_i \mathcal{X}_\mu(r_i) H_{eff}(r_i)\, \mathcal{X}_\upsilon(r_i) \omega(r_i) \qquad (29)$$

$$S_{\mu\nu} \cong \sum_i \mathcal{X}_\mu(r_i)\, \mathcal{X}_\upsilon(r_i) \omega(r_i) \qquad (30)$$

The sums run over several numerical integration points r_i. The term $H_{eff}(r_i)$ represents the value of the integrand at point r_i and $w(r_i)$ represents a weight associated with each mesh point. Increasing the number of mesh points improves the numerical precision of the integral but also results in additional computational cost.

The integration points are generated in a spherical pattern around each atomic center. Radial points are typically taken from the nucleus to an outer distance of 5.5 Å (~10.4 Bohr). The number of radial points within this distance is designed to scale with the increasing atomic number. For example, Fe requires more points than C. The typical number of radial points N_R for a nucleus of charge Z is calculated with eq. 31.

$$N_R = 14(Z+2)^{1/3} \qquad (31)$$

Partition functions are used to increase the convergence of the numerical integration and to avoid integrating over nuclear cusps. A partition function ρ_α is defined with eq. 32 as follows:

$$\rho_\alpha(r) = \frac{g_\alpha(r-R_\alpha)}{\sum_\beta g_\beta(r-R_\beta)} \qquad (32)$$

Where α is an atom index, g_α(**r**-**R**$_\alpha$) is a function that typically is large for small **r**-**R**$_\alpha$ and small for large **r**-**R**$_\alpha$ (that is, larger near the nucleus). Integrals are rewritten using partition functions as in eq. 33:

$$\int f(r)dr = \sum_\alpha f(r)\rho_\alpha(r)dr \qquad (33)$$

which is further reduced to a sum over integration points such as in eq. 34:

$$\sum_\alpha \int f(r)\rho_\alpha(r)dr \cong \sum_\alpha \sum_i f(r_i)\rho_\alpha(r_i)\,\omega\,(r_i) \qquad (34)$$

The partition functions are combined with the integration weights w(r_i) to simplify the computation. The choice for a partition function for the geometrical optimization of chitosan is shown in eq. 11:

$$g_\alpha(r) = \rho_\alpha(r)\left\{e^{-r_0/r} - 1 - \frac{r_0}{r}\right\} \qquad (35)$$

The SimulaTEM® program is based on the use of the multilayer method of Cowley and Moody [19] used as the theoretical basis for the program, which represents images from transmission electron microscopy (TEM) for non-crystalline models of condensed matter structures in the PDB format (Protein Database [20]). This formulation assumes that the flow of electrons passing across the sample is represented by the electronic transmission through a set of N objects of amplitude and phase, separated by a distance Δz. The total changes in amplitude and phase of the incident wave that occur on the first objects are considered to occur on a crystallographic plane. The propagation of this wave towards the next plane will be given by the Fresnel approximation (eq. 35). For the limiting case in which the thickness of the object Δz tends to zero and the number of objects tends to infinity, if H is the total thickness of the set of objects, and NΔz=H is the description of the phenomenon, then it becomes a rigorous representation of electron scattering consistent with the description given by quantum mechanics.

$$\phi(x,y,z) = \iint du\,dv\,A(u,v)e^{2\pi\left(ux+vy+z(\chi^2-u^2-v^2)^{1/2}\right)} \qquad (36)$$

For the implementation of Cowley's method, no approximations were performed with respect to the thickness Δz; that is, the integral of the potential across the cut is not approximated by

an integral from –∞ to +∞, as is often assumed elsewhere [15]. The propagator is taken without approximations on the square root that appears in its definition; neither is a small angle approximation made, nor is any assumption made regarding the crystallinity of the sample. The algorithm used is designed from the start in such a way that it can handle arbitrary objects and its only limitation is the mosaic effect implicit in the use of the discrete Fourier transform algorithm of the general solution described in eq. 37.

$$\phi(x,y,z) = T(x,y) \iint du\, dv\, A(u,v) e^{2\pi\left(ux+vy+z(X^2-u^2-v^2)^{1/2}\right)} \tag{37}$$

In the Layers subroutine, the scattering object is divided into N layers of the same thickness, Δz, as shown in Figure 4. Applying the Fourier transform in eq. 37 and using eq. 36, it becomes eq. 38:

$$\mathcal{F}[\phi(x,y,z)] = \mathcal{F}[T(x,y)] * \left[\mathcal{F}[\phi(x,y,0)]\mathcal{F}[Pz(x,y)]\right] \tag{38}$$

By obtaining the inverse transform of eq. 37 we will have eq. 39:

$$\phi(x,y,z) = T(x,y)\,[\phi(x,y,0) * Pz(x,y)] \tag{39}$$

The diagram of the main program is schematized in Figure 1.

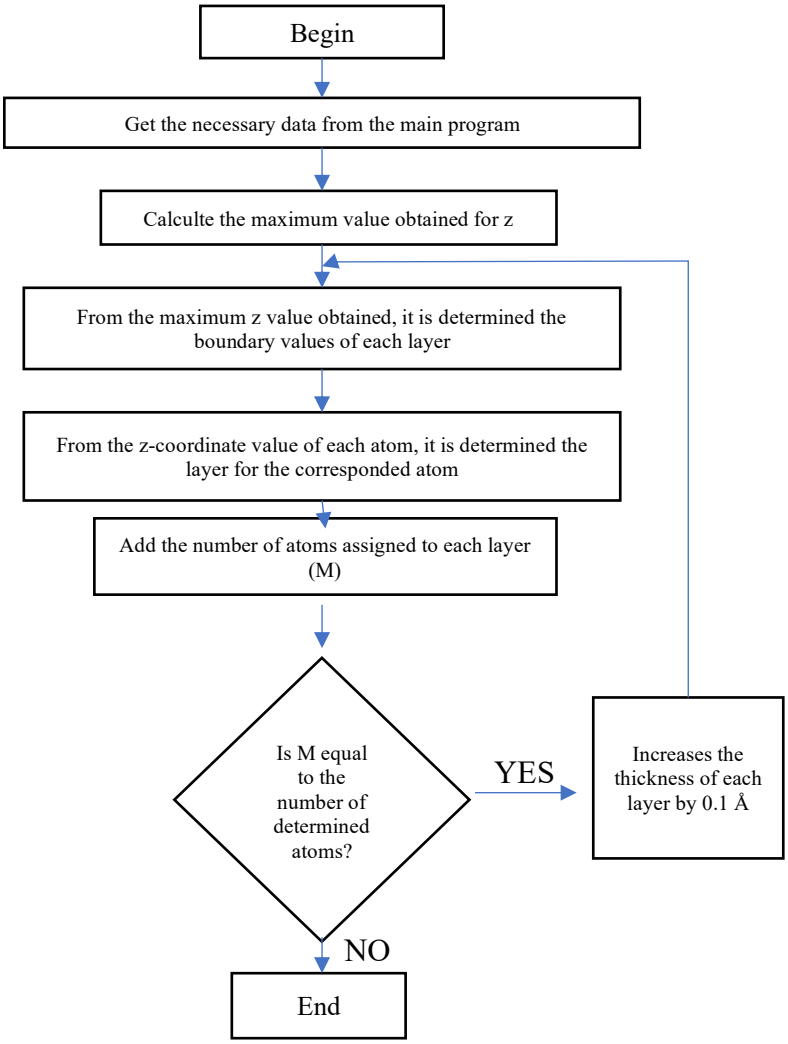

Figure 1. Diagram of process for the calculation of an TEM image by the multilayer method [20] used in SimulaTEM software.

MD simulation

In Material Studio®, the Forcite module includes different force fields and their functional forms are included in the help pages of the software. Many force fields include van der Waals and electrostatic interactions for all pairs of atoms and angles in their entirety, while others scale the interaction by a fixed numerical factor (typically 0.5). The following equation is an example of the general forcefield function corresponding to the COMPASS module of Materials Studio®:

$$V(R) = \sum_{b} D_b\left[1 - e^{-a(b-b_0)}\right]^2 + \sum_{\theta} H_\theta(\theta - \theta_0)^2 + \sum_{\phi} H_\phi[1 - s\cos(n\phi)]$$
$$+ \sum_{\chi} H_\chi \chi^2 + \sum_{b}\sum_{b'} F_{bb'}(b - b_0)(b' - b_0') + \sum_{\theta}\sum_{\theta'} F_{\theta\theta'}(\theta - \theta_0)(\theta' - \theta_0')$$
$$+ \sum_{b}\sum_{\theta} F_{b\theta}(b - b_0)(\theta - \theta_0) + \sum_{\phi} F_{\phi\theta\theta'}\cos(\theta - \theta_0)(\theta' - \theta_0')$$
$$+ \sum_{\chi}\sum_{\chi'} F_{\chi\chi'}\chi\chi' + \sum_{i}\sum_{j>i}\left[\frac{A_{ij}}{r_{ij}^{12}} - \frac{B_{ij}}{r_{ij}^{6}} - \frac{q_i q_j}{r_{ij}}\right] \quad (40)$$

The first four terms of Eq. 40 are sums reflecting the energy required for: stretching bonds (b) angles (θ), torsion angles (φ), atoms around the bond axis determining the torsion angle out of the plane formed by the atoms to which they are bonded (χ).

The following five terms are cross terms that explain the interactions between the four types of internal coordinates.

The final term represents the non-bonding interactions as a sum of repulsive and attractive Lennard-Jones terms, as well as Coulomb terms, all of which are a function of the distance (r) between pairs of atoms (i,j).

The force field defines the functional form of each term in this equation, as well as the D, a and b parameters. It also defines the internal coordinates as a function of the Cartesian atomic coordinates, b_0.

Once the force field types have been defined for all particles in the simulation, the Forcite parameter assignment engine can use them to locate the correct parameters for a given term in the energy expression. Schematically it can be seen in the Figure 2 that the following can

be assigned to each type of atom.

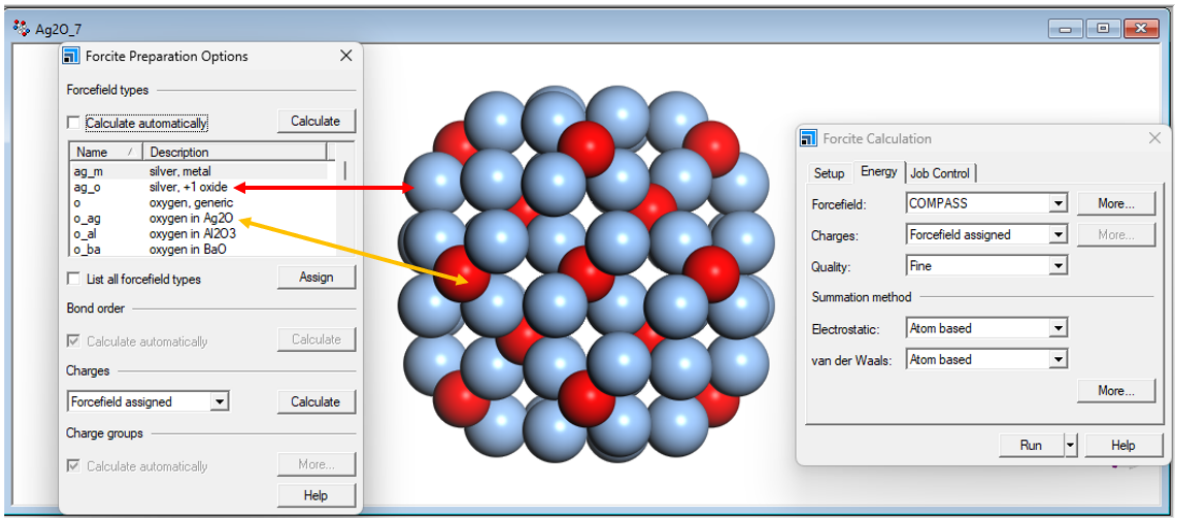

Figure 2. Mapping scheme of atom types in the COMPASS force field of forcite.

There are two types of bonds ag_m (silver-metal) and ag_o (silver-oxide). There will be terms corresponding to each bond in the energy expression, but the parameters used in these terms will depend on the combination of force field types.

In addition to the bond terms, there are angle, torsion and other terms and the parameters that are assigned for these terms are also determined by the combination of force field types that make up the term; each of which may have a different set of associated parameters and possibly even a different functional form.

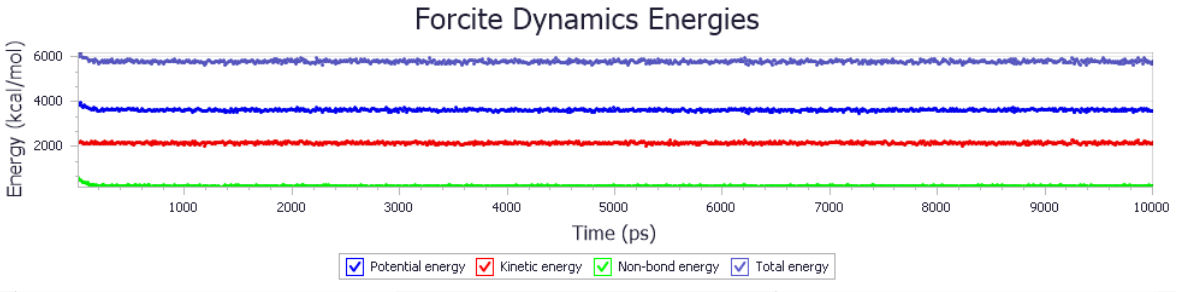

The system equilibrium

Figure 3. Energy of Forcefield COMPASS.

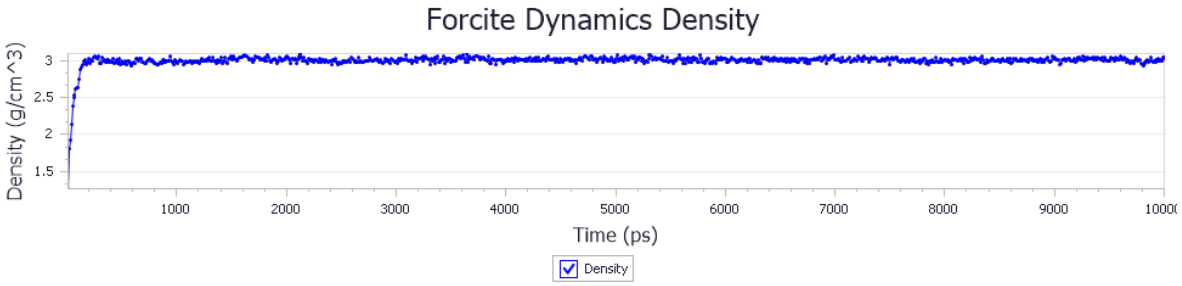

Figure 4. Density of the system.

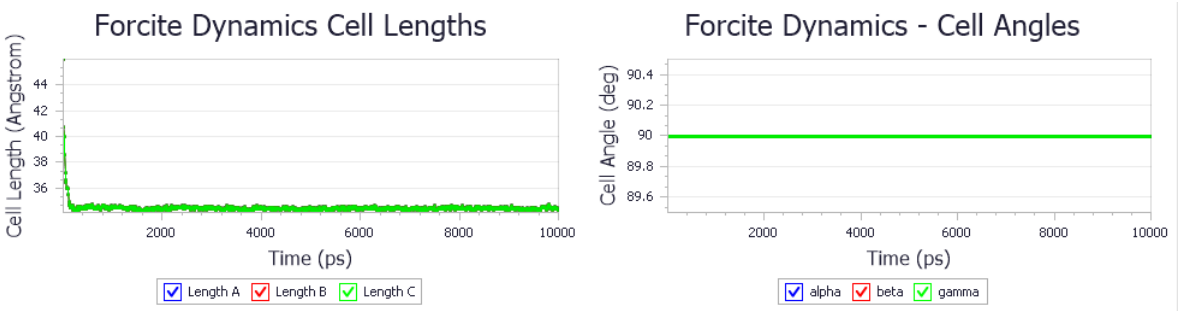

Figure 5. Lengths and angles of the system.

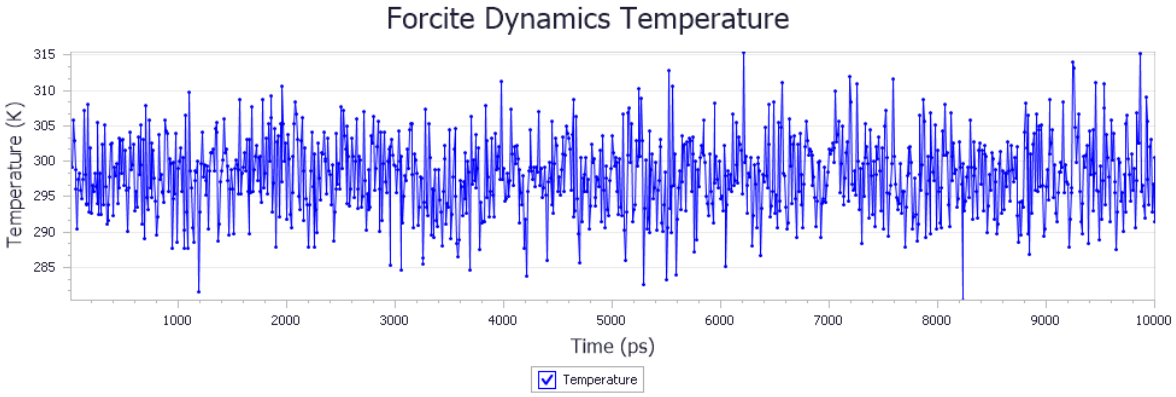

Figure 6. Temperature of the system.

References

[1] M.J.S. Dewar, Development and status of MINDO/3 and MNDO, J. Mol. Struct., 100, (1983) 41-50. https://doi.org/10.1016/0022-2860(83)90082-0.

[2] J.C. Slater, (1972). Statistical Exchange-Correlation in the Self-Consistent Field. Advances in Quantum Chemistry, 1–92. doi:10.1016/s0065-3276(08)60541-9.

[3] Andrzej Wolski, Theory of electromagnetic fields (Liverpool U. and Cockcroft Inst. Accel. Sci. Tech.) (Nov, 2011) Contribution to: CERN Accelerator School: Course on RF for Accelerators • e-Print: 1111.4354 [physics.acc-ph]

[4] C.C.J Roothaan, New developments in molecular orbital theory, Rev. Mod. Phys. 23 (1951) 69-89. https://doi.org/10.1103/RevModPhys.23.69.

[5] P. Hohenberg, W. Kohn, Inhomogeneous electron gas, Phys. Rev. B, 136 (1964) 864-871. https://doi.org/10.1103/PhysRev.136.B864.

[6] J.E. Inglesfield, Theory of the inhomogeneous electron gas, Phys. Bull. 35 (1983) 201-202. DOI 10.1088/0031-9112/35/5/023.

[7] M. Levy, Universal variational functionals of electron densities, first-order density matrices, and natural spin-orbitals and solution of the v-representability problem, Proc. Natl. Acad. Sci. U. S. A. 76 (1979) 6062-6065. https://doi.org/10.1073/pnas.76.12.6062.

[8]J.A. Pople, R.K.J. Nesbet Self-consistent orbitals for radicals, Chem. Phys. 22 (1954) 571-572. https://doi.org/10.1063/1.1740120.

[9] L. Hedin, B.I. Lundqvist, Explicit local exchange correlation potentials, J. Phys. C. 4 (1971) 2064-2083. DOI 10.1088/0022-3719/4/14/022.

[10] D.M. Ceperley, B.J. Alder, Ground state of the electron gas by a stochastic method, Phys. Rev. Lett. 45 (1980) 566-569. https://doi.org/10.1103/PhysRevLett.45.566.

[11] J.F. Lutsko, Generalized expressions for the calculation of elastic constants by computer simulation, J. App. Phys. 65 (1989) 2991-2992. https://doi.org/10.1063/1.342716.

[12] J. Andzelm, E. Wimmer, D.R. Salahub, Spin density functional approach to the chemistry of transition metal clusters: Gaussian-type orbital implementation, in D.R. Salahub, M.C. Zerner (Eds) The Challenge of d- and f-Electrons: Theory and Computation, ACS Symp. Ser., Ser. 394, 1989, pp. 228-245. DOI 10.1021/bk-1989-0394.ch016.

[13] L. Versluis, T. Ziegler, The determination of molecular structures by density functional theory. The evaluation of analytical energy gradients by numerical integration, J. Chem. Phys. 88 (1988) 322-328. https://doi.org/10.1063/1.454603.

[14] M.C. Payne, M.P. Teter, D.C. Allan, T.A. Arias, J.D. Joannopoulos, Iterative Minimization Techniques for Ab Initio Total Energy Calculations: Molecular Dynamics and Conjugate Gradients, Rev. Mod. Phys. 64 (1992), 1045-1097. https://doi.org/10.1063/1.454603.

[14] M.J.S. Dewar, Development and status of MINDO/3 and MNDO, J. Mol. Struct., 100, (1983) 41-50. https://doi.org/10.1016/0022-2860(83)90082-0.

[15] J.C. Slater, (1972). Statistical Exchange-Correlation in the Self-Consistent Field. Advances in Quantum Chemistry, 1–92. doi:10.1016/s0065-3276(08)60541-9.

[16] S.H. Vosko, L. Wilk, M. Nusair, Accurate spin-dependent electron liquid correlation energies for local spin density calculations: A critical analysis, Can. J. Phys. 58(1980) 1200-1211 (1980). https://doi.org/10.1139/p80-159.

[17] J.P. Perdew, JY. Wang, (1992). Accurate and simple analytic representation of the electron-gas correlation energy. Physical Review B, 45(23), 13244–13249. doi:10.1103/physrevb.45.13244. https://doi.org/10.1103/PhysRevB.45.13244.

[18] B. Delley, Time dependent density functional theory with DMol3, J. Phys. Condens. Matter, 22, (2010) 384208-384210. DOI 10.1088/0953-8984/22/38/384208.

[19] J.M. Cowley, A.F. Moodie, The scattering of electrons by atoms and crystals. III. Single-crystal diffraction patterns. Acta Crystallographica, 12 (1959) 353-359. doi:10.1107/S0365110X59001104.

[20] Bioinformatics of green fluorescent protein. Protein data bank. www.rcsb.org, 2015 (accessed 02 March 2023).

[21] R. Herrera, Un Algoritmo para la Simulación de Imágenes y patrones de difracción de objetos arbitrarios en Microscopia Electrónica de Alta Resolución, Ph.D. Disertación, C.I.C.E.S.E, Ensenada, México, 1989.